ELSEVIER

Contents lists available at ScienceDirect

Corrosion Science

journal homepage: www.elsevier.com/locate/corsci





Improved corrosion resistance of cathodic arc evaporated $Al_{0.7}Cr_{0.3-x}V_xN$ coatings in NaCl-rich media

O.E. Hudak ^{a,*}, P. Kutrowatz ^a, T. Wojcik ^a, E. Ntemou ^b, D. Primetzhofer ^b, L. Shang ^c, J. Ramm ^c, O. Hunold ^c, S. Kolozsvári ^d, P. Polcik ^d, H. Riedl ^{a,e}

- ^a Christian Doppler Laboratory for Surface Engineering of high-performance Components, TU Wien, Austria
- ^b Department of Physics and Astronomy, Uppsala University, 75120 Uppsala, SE, Sweden
- ^c Oerlikon Balzers, Oerlikon Surface Solutions AG, 9496 Balzers, Liechtenstein
- ^d Plansee Composite Materials GmbH, D-86983 Lechbruck am See, Germany
- e Institute of Materials Science and Technology, TU Wien, A-1060 Wien, Austria

ARTICLE INFO

Keywords:
PVD coatings
Cathodic arc evaporation
Pitting
Corrosion resistance
Open porosity

ABSTRACT

The corrosion resistance of cathodic arc evaporated $Al_{0.7}Cr_{0.3-x}V_xN$ coatings with a vanadium content up to 22.3 at% has been electrochemically tested in a 0.1 M NaCl-solution. Significant improvement in the open porosity and corrosion rate was observed for coatings with higher V-contents, due to a denser and more refined coating morphology. Further reduction in the open porosity rate was achieved through an annealing step in air at 700 °C. Here, the formation of an AlVO₄ top-oxide and underlying oxygen-rich V-depletion zone provides additional sealing of the coating surface, whilst reducing the corrosion current density to a final 1.59×10^{-9} A/cm².

1. Introduction

One of the biggest drawbacks regarding the application of corrosion protective PVD coatings on bulk materials (e.g. steels) is the presence of open porosities. Pores or defect sites (e.g. embedded macroparticles, porosity due to highly orientated columnar growth, pin holes, etc.) allow the corrosive medium to travel unhindered to the coating/substrate interface and generate galvanic couples [1–3]. Depending on the materials that make up this galvanic cell, coatings may either act as the anodic element (providing sacrificial protection) [4], or act as the cathodic element, in which anodic dissolution and pitting of the substrate material ensues [5]. For the latter case, which pertains to most ceramic protective coatings, the coating itself remains inert, whereas the steel underneath suffers detrimental corrosion [6–11].

In recent years, a great number of strategies have been pursued to minimize the open-porosity values in protective PVD coatings and limit the probability of the electrolyte to make contact with less noble substrates. Whether this is achieved by: i) increasing the coating thickness [12–14], ii) incorporating a dense interlayer between the substrate and coating (interlayer designs) [6,7,15,16], iii) disrupting the columnar growth orientation by means of multilayer architectures [17–20], or iv) by refining the coating morphology altogether through alloying routs

[21], all approaches aim to obstruct fast-track diffusion pathways between the electrolyte and the substrate in order to improve the corrosion behavior of the system.

Following a doping strategy, this study provides novel insights into the positive impact that V-doping imparts on the corrosion behavior of cathodic arc evaporated AlCrN thin films in NaCl-rich media. An Al $_{0.7}$ Cr $_{0.3}$ N chemistry was chosen as the base system, whereupon chromium was progressively substituted with vanadium. In a series of Al $_{0.7}$ Cr $_{0.3-x}$ V $_x$ N depositions, with vanadium contents ranging from x = 0–22.3 at% on the metal sublattice, two strategies are being pursued: *i*) improving the corrosion behavior solely by means of vanadium-doping, and ii) further improving the corrosion resistance of the Al $_{0.7}$ Cr $_{0.3-x}$ V $_x$ N series through an annealing step and consequent development of a vanadium-rich top-oxide scale. Thus, the first part of this study will focus on the effect of vanadium content in the as-deposited state, by considering changes in microstructure and crystal phase composition, while the second part will provide a detailed investigation on the oxide scale formation and diffusion mechanisms of the annealed samples.

2. Experimental methods

All coatings were deposited in an industrial scale deposition system

^{*} Correspondence to: TU Wien- Institute of Materials Science and Technology Getreidemarkt 9/ E308-01, A-1060 Wien, Österreich E-mail address: oliver.hudak@tuwien.ac.at (O.E. Hudak).

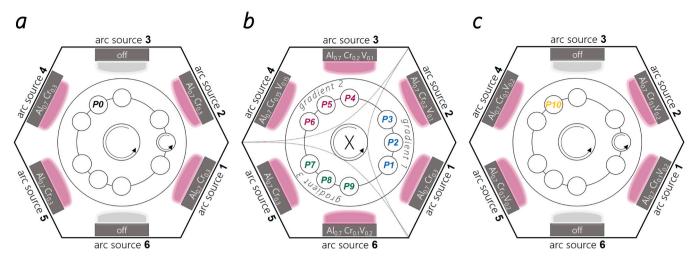


Fig. 1. : Schematic of the cathodic arc evaporation deposition chamber, showing target arrangements, sample positions used for all $Al_{0.7}Cr_{0.3-x}V_xN$ coatings. a) shows a rotary deposition run equipped with $Al_{0.7}Cr_{0.3}$ targets (P0). b) shows a stationary deposition run with varying target arrangements used for P1-P9. Gradient 1 (P1-P3) was placed between $Al_{0.7}Cr_{0.3}$ and $Al_{0.7}Cr_{0.2}V_{0.1}$ targets, Gradient 2 (P4-P5) was placed between $Al_{0.7}Cr_{0.2}V_{0.1}$ and $Al_{0.7}Cr_{0.1}V_{0.2}$ targets, and Gradient 3 (P7-P9) was positioned between $Al_{0.7}Cr_{0.3}$ and $Al_{0.7}Cr_{0.1}V_{0.2}$ targets. c) shows a rotary deposition run equipped with $Al_{0.7}Cr_{0.1}V_{0.2}$ targets (P10).

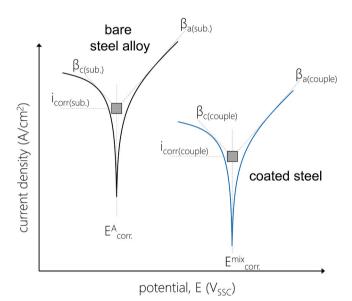


Fig. 2. : A schematic of a Tafel Plot from which several electrochemical parameters can be obtained: $E_{corr.}^{A}$, corrosion potential of the bare steel; $E_{corr.}^{mix}$ mixed corrosion potential of the deposited coatings on steel; $i_{corr.}$ corrosion current density; $\beta_{c(alloy),}$ $\beta_{a(alloy),}$ cathodic and anodic Tafel-slopes of the bare alloy; $\beta_{c(couple)}$, $\beta_{a(couple)}$, cathodic and anodic Tafel-slopes of the coating-alloy couple.

(INNOVA, Oerlikon Balzers, Liechtenstein) by cathodic arc evaporation. Al $_{0.7}$ Cr $_{0.3-x}$ V $_x$ targets were powder-metallurgically manufactured by Plansee Composite Materials GmbH and used for all coating variants. Steel foil with 0.05 mm thickness, and low-alloy steel discs (90MnCrV8) were utilized as substrates. Whereas the steel-foil was solely appropriated for as-deposited characterization purposes (e.g. analysis of the coatings morphology via fracture cross-section, coating thickness measurements and crystal-phase investigations by X-ray diffraction), the coated steel discs were exclusively used for electrochemical-corrosion experiments and post-corrosion analysis. All substrates were ultrasonically cleaned in acetone and ethanol before they were mounted into the deposition chamber. With a base pressure of $< 5.0^{-4}$ Pa, the substrates were further cleaned for 25 min by an argon plasma etching procedure (Oerlikon Surface Solutions AG).

All arc evaporated coatings were deposited in a pure N2 atmosphere

at 3.5 Pa, with a DC-bias of up to - 100 V at 480 $^{\circ}\text{C}.$ Regarding the corrosion behavior, all coatings were grown to a thickness $\sim\!\!5~\mu m$ for optimal comparison.

2.1. Gradient coating procedure

Fig. 1 shows the schematic of the deposition chamber equipped with six arc-sources. A total of 11 $Al_{0.7}Cr_{0.3-x}V_xN$ coatings with varying V-content were deposited (designated P0-P10, by using several target compositions: $Al_{0.7}Cr_{0.3}$, $Al_{0.7}Cr_{0.2}V_{0.1}$, $Al_{0.7}Cr_{0.15}V_{0.15}$ and $Al_{0.7}Cr_{0.1}V_{0.2}$ at%.

P0 designates the $Al_{0.7}Cr_{0.3}$ V_xN base coating with the lowest V-content (0 at% V). The deposition system was equipped with four $Al_{0.7}Cr_{0.3}$ targets and operated with a two-fold substrate rotation, as shown in Fig. 1a.

P1-P9 represent $Al_{0.7}Cr_{0.3-x}V_xN$ coatings with varying V-contents that come from a stationary deposition mode (no substrate rotation). Three substrates were placed between two adjacent arc sources, equipped with different target compositions, as shown in Fig. 1b. Depending on the V content of each target, together with the relative distance of the substrates to each of the two respective arc-sources, a slightly different coating composition was obtained.

P10 denotes the $Al_{0.7}Cr_{0.3-x}V_xN$ coating with the highest V-content. The deposition system was equipped with four $Al_{0.7}Cr_{0.1}V_{0.2}$ targets and operated with a two-fold substrate rotation (Fig. 1c).

2.2. Annealing experiments in air

Isothermal annealing experiments were conducted in air at 700 $^{\circ}\text{C}.$ For each treatment, the chamber furnace (Medlin & Naber GesmbH, Vienna, Austria) was preheated to 700 $^{\circ}\text{C}$ and let equilibrate for a minimum of 12 h. All temperature profiles were monitored using a Naber Temperature TP1 processor in conjunction with a mounted type K thermoelement. The coated samples were then placed into the preheated chamber and annealed isothermally for 3 h.

2.3. Characterization of as-deposited and annealed coatings

For studying the morphology of the coatings (coating thickness, surface texture, and the integrity of the substrate-coating interfaces), a Zeiss Sigma 500 VP high-resolution field emission gun scanning electron microscope (FEGSEM) was used. With an acceleration voltage, ranging between $3~\rm kV$ and $7~\rm kV$, characterization of coating thickness and

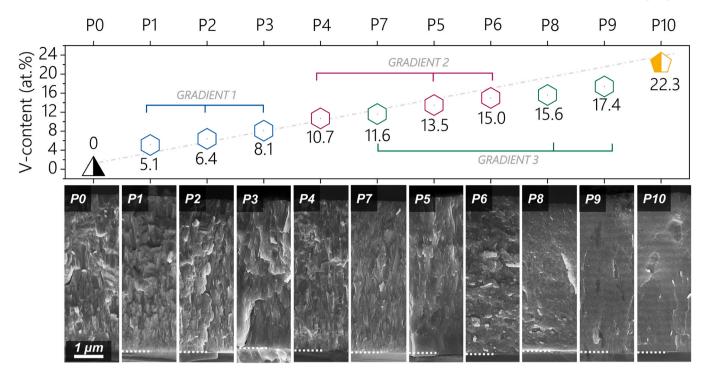


Fig. 3. : SEM micrographs showing fracture cross-sections of as-deposited $Al_{0.7}Cr_{0.3-x}V_xN$ with varying vanadium contents (P0 to P10). Their respective vanadium contents (at% on the metal sublattice) are presented above.

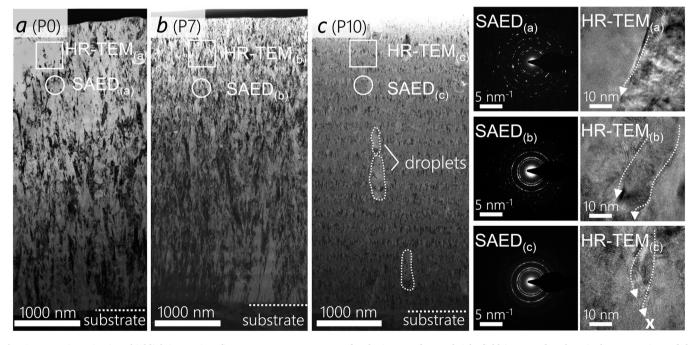


Fig. 4.: TEM investigations highlighting grain-refinement, as a consequence of V-doping. a-c feature bright-field images of as-deposited cross sections of the $Al_{0.7}Cr_{0.3}N$, $Al_{0.7}Cr_{0.19}V_{0.11}N$ and $Al_{0.7}Cr_{0.08}V_{0.22}N$ coatings, respectively. Further SAED and HR-TEM images render information about the crystallinity, as well as manifestation of grain-boundaries that comprise the coating matrix.

coating morphology were performed on fracture cross sections of coated steel-foil substrates. Equipped with an EDAX Octane elect system, energy dispersive X-ray spectroscopy (EDX) was utilized for quantitative elemental investigations.

Complementary to the EDX measurements, Time-of-Flight Heavy Ion Elastic Recoil Detection Analysis (ToF-HIERDA) was employed. All measurements were performed at the 5 MV 15SDH-2 Pelletron tandem accelerator at Uppsala University [22] employing $^{127}\mathrm{I}^{8+}$ projectiles with

a primary energy of 36 MeV with an incident angle of 67.5° with respect to the surface normal and a recoil detection angle of 45° with respect to the incident beam direction. Elemental composition depth profiles were determined using the CONTES software package [23] with the total systematic and statistical uncertainties estimated to be below 5% of the deduced value for the major constituents. For a more detailed description of the analytical set-up, we refer the reader to Ström et. al. [24].

For a more detailed investigation of the coating morphologies,

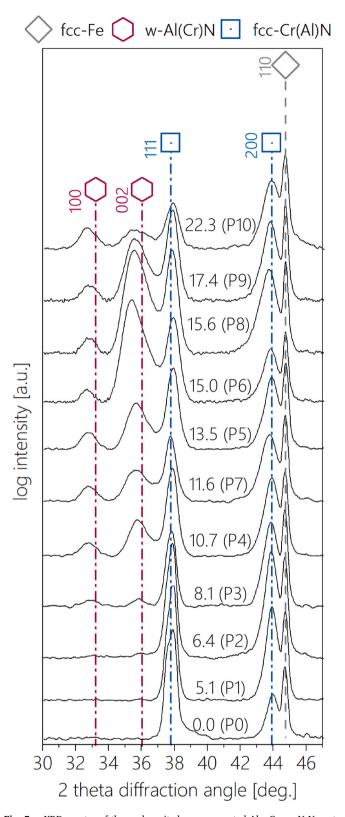
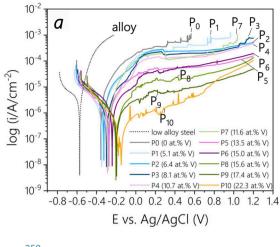


Fig. 5. : XRD spectra of the as-deposited arc evaporated $Al_{0.7}Cr_{0.3-x}V_xN$ coatings with increasing V-contents (at% V on the metal sublattice). Reference patterns were taken from Ref. [25–27].

transmission electron microscopy (TEM, FEI TECNAI F20, equipped with a field emission gun and operated at an accelerating voltage of 200 kV) was conducted. Bright field (BF) imaging was utilized to learn more about the microstructure, crystallinity, and texture. For the



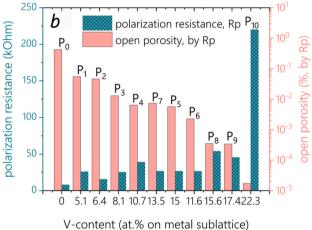


Fig. 6. : Electrochemical investigations of as-deposited $Al_{0.7}Cr_{0.3-x}V_xN$ coatings with varying vanadium-content (at% V on metal sublatice): a) Shows the original Tafel-plots measured in 0.1 M NaCl-solution, from which b) polarization resistance and open porosity values were calculated.

preparation of the TEM lamellas, a standard lift-out procedure during focused-ion beam etching (FIB) milling was utilized (Scios 2 DualBeam system, ThermoFisher Scientific).

For crystallographic investigations, Bragg-Brentano X-ray diffraction (BBHD) was utilized, using a PANalytical XPert Pro MPD system equipped with a Cu-K α radiation source (wave length $\lambda=1.54$ Å).

Electrochemically corroded samples were embedded in a conductive polymer-matrix, their cross-sections ground and polished, and analyzed via SEM and EDX. Accordingly, pit-formations, coating-substrate adherence, and fast-track diffusion routes of the electrolyte were examined.

2.4. Electrochemical corrosion experiments

Linear potentiodynamic polarization experiments were performed using a three-electrode set-up. With a saturated Ag/AgCl reference electrode (SSC), a Pt-counter electrode (CE) and the coated steel sample as working electrode (WE), the electrochemical experiments were conducted in a 0.1 M NaCl solution. Each sample was mounted into a pressfit corrosion cell, which accommodated a sample contact area of 1.58 cm. All samples were left to equilibrate for 20 min, after which the corrosion potential (Ecorr.) was measured. Once the measured potential drops below a time derivative limit (dE/dt= $1\times 10^{-6} \, \text{V/s}$), the recorded potentials from the last 5 s was averaged and taken as E_{corr} . The linear sweep voltammetry (LSV) measurements were started cathodically at E_{corr} . $-300 \, \text{mV}$ and swept into the anodic region with a sweep-rate of

Table 1 Electrochemical properties of as-deposited $Al_{0.7}Cr_{0.3-x}V_xN$ coated low-alloy steel substrates in 0.1 M NaCl solution. $E_{corr.}$, corrosion potential; I_{pass} , passive current density; i_{corr} , corrosion current density; β_c , cathodic Tafel-slope; β_a , anodic Tafel-slope; R_p , polarization resistance; P_{Rp} , open porosity deduced from R_p .

material	V-content on metal- sublattice (at%)	$E_{corr.}$ (mV)	$I_{pass.}$ (A/cm^2)	I_{corr} (A/cm^2)	β_c (mV/dec)	β _a (mV/dec)	R_p $(k\Omega \times cm^2)$	P _{Rp} (%)
low-alloy steel	n.a.	-560	n.a.	3.17×10 ⁻⁶	363.6	76.9	8.6	n.a.
AlCrN	0 (P0)	<i>-375</i>	$6.60 \times 10^{-4} \pm 1.12 \times 10^{-4}$	2.57×10^{-6}	115.7	81.7	8.0	4.22×10^{-1}
$Al_{0.7}Cr_{0.3-x}V_xN$	5.1 _(P1)	-344	$4.03 \times 10^{-4} \pm 3.00 \times 10^{-5}$	8.50×10^{-6}	129.4	84.7	25.9	5.48×10^{-2}
as-deposited	6.4 _(P2)	-323	$2.45 \times 10^{-4} \pm 1.51 \times 10^{-5}$	1.64×10^{-6}	191.2	85.1	15.4	4.61×10^{-2}
	8.1 _(P3)	-297	$1.94 \times 10^{-4} \pm 1.52 \times 10^{-5}$	9.69×10^{-7}	146.0	93.6	25.3	1.29×10^{-2}
	10.7 _(P4)	-288	$1.38{ imes}10^{-4}~{\pm}5.85{ imes}10^{-6}$	5.93×10^{-7}	150.4	84.4	39.1	6.38×10^{-3}
	11.6 _(P7)	-280	$1.33{ imes}10^{-4}~{\pm}9.77{ imes}10^{-6}$	6.89×10^{-7}	109.6	69.4	26.6	7.39×10^{-3}
	13.5 _(P5)	-271	$5.36 \times 10^{-5} \pm 2.89 \times 10^{-6}$	9.43×10^{-7}	178.6	86.7	26.6	5.65×10^{-3}
	15.0 _(P6)	-240	$6.02 \times 10^{-5} \pm 3.07 \times 10^{-6}$	9.85×10^{-7}	135.7	109.6	26.4	2.24×10^{-3}
	15.6 _{(P8})	-202	$\begin{array}{l} 1.99 \times 10^{-5} \\ \pm 2.31 \times 10^{-6} \end{array}$	5.41×10^{-7}	149.0	125.0	53.9	3.52×10^{-4}
	17.4 _(P9)	-195	$9.08 \times 10^{-6} \pm 4.25 \times 10^{-7}$	3.68×10^{-7}	77.3	78.6	45.5	3.39×10^{-4}
	22.3 _(P10)	-148	$4.07 \times 10^{-6} \ \pm 6.64 \times 10^{-7}$	$1.03{ imes}10^{-7}$	151.3	81.1	220.0	1.72×10^{-4}

1~mV/s up to $+1.2~\text{V}_{SSC}$. With a current-density cut-off value set to $1~\text{mA/cm}^2$, the electrochemical tests were controlled and monitored by a potentiostat (Autolab PGSTAT302N, Metrohm).

2.5. Deductions based on polarization measurements

Since protective coatings are prone to coating defects or open porosities, the measured galvanic current densities of the coated steel samples will depend on the contact ratio of the electrolyte and the coating/substrate surfaces. In other words, when the electrolyte is brought in contact with a "porous" coating surface, part of the electrolyte will contact the coating and part of the substrate material beneath, generating a galvanic couple.

From the Tafel-plots, the cathodic and anodic Tafel-slopes (β_c and β_a), as well as corrosion current density values (i_corr) and corrosion potential (E_corr.) were extrapolated (see Fig. 2). By using the Stern-Geary Equation (see Eq. 1), the polarization resistance (R_p) could be calculated for the uncoated substrate, as well as all Al_0.7Cr_{0.3-x}V_xN coated samples.

Stern – Geary Equation(
$$R_p$$
) = $\frac{\beta_c * \beta_a}{2.33 * i_{corr}(\beta_c + \beta_a)}$ (1)

Finally, according to the following relation (Eq. 2), the porosity of the coating was calculated:

$$P = \frac{R_{p(substrate)}}{R_{p(coating)}} * 10^{-(\frac{|\Delta E_{corr}|}{\sigma_{a(substrate)}})}$$
 (2)

where P denotes the open porosity of the coating, $R_{p(substrate)}$ is the polarization resistance of the uncoated substrate material, $R_{p(coating)}$ is the polarization resistance of the coated substrate, $\Delta E_{corr.}$ refers to the difference in the corrosion potential between the uncoated and coated substrate, and $\beta_{a(substrate)}$ to the anodic Tafel-slope of the bare substrate – also see Fig. 2.

Lastly, by combining the corrosion current density (I_{corr}) with Faraday's Law (see Eq.3), the corrosion rate (CR) may be calculated (see Eq.4).

$$W = \frac{A_w Q}{zF} \tag{3}$$

where W is the mass material removed, $A_{\rm w}$ is the atomic weight of the sample, Q is the total charge passed through the system and z is the number of electrons transferred in the reaction.

$$CR = W * \frac{As}{\rho} \tag{4}$$

where A_s is the exposed surface area and ρ is the density of the material.

3. Results and discussion

3.1. Microstructure and composition analysis

The as-deposited microstructures of all $Al_{0.7}Cr_{0.3-x}V_xN$ coatings are shown in Fig. 3. The fracture cross section labeled P0 represents the as-deposited microstructure of the base system $Al_{0.7}Cr_{0.3}N$ with 0 at% vanadium. We would like to point out that this coating does not come from a stationary deposition run, but instead was deposited in a conventional manner with rotation and four identical target compositions. P1 to P9, on the other hand, do originate from the stationary gradient deposition and are numerated according to the arrangement within the chamber (revisit Fig. 1). P10 represents the microstructure of the coating with the highest V-content and was also deposited with substrate rotation and four identical $Al_{0.7}Cr_{0.1}V_{0.2}$ targets mounted within the deposition chamber. Above the cross-sectional SEM images the corresponding V-contents are plotted (at% on the metal sublattice, determined by EDX and verified by ERDA). For a complete overview of the chemical compositions, we refer to Appendix A.

First observations of the as-deposited microstructures indicate a gradual grain-refinement with increasing vanadium content. While a distinct columnar growth morphology exists for chemistries ≤ 10.7 at% of V on the metal sublattice (P0-P3), a reduction in the column sizes can be noticed for contents ≥ 10.7 but ≤ 15.0 at% (P4, 5 and 7). From 15.0 at% upwards, the microstructure transitions into a coarse grained microstructure (P6 and P8) after which a featureless morphology predominates (P9 and P10).

TEM investigations further substantiate these observations. Fig. 4 shows the bright-field cross-sections of the as-deposited coatings P0, P7 and P10 with V-contents of 0, 11.6 and 22.3 at%, respectively (at% V on metal sublattice). Standing in good agreement with the previously shown SEM images, the effect of grain-refinement is clearly visible as the vanadium content increases. An initial refinement of the columnar structure is observed between P0 and P7, after which a featureless morphology develops. Selected area electron diffractograms (SAED), as well as high resolution TEM (HR-TEM) images were collected near the coating surfaces, to provide localized information about the coatings' crystallinity. Starting with the Al_{0.7}Cr_{0.3}N coating with 0 at% V-content (P0), the SAED_(a) provides a diffraction pattern with distinct diffraction dots, which is indicative of a crystalline morphology. The respective HR-TEM(a) image features a well-defined column-boundary, which would, in case of a subsequent corrosion experiment, offer a preferential diffusion path for chloride species. Such fast track diffusion pathways for chloride species have been investigated in a previous study [1], and deemed to be a significant draw-back in effectively providing corrosion protection. As vanadium is substituted for chromium, first to 11.6 at% (P7) and then further to 22.3 at% V-content (P10), the SAEDs feature

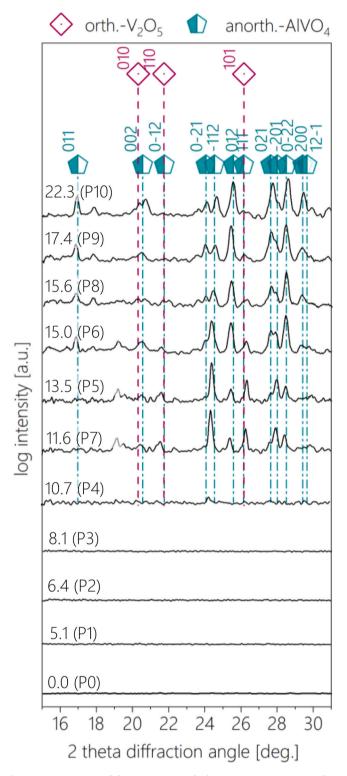


Fig. 7.: XRD spectra of the arc evaporated $Al_{0.7}Cr_{0.3-x}V_xN$ coatings isothermally annealed at 700 °C in air for 3 h with increasing V-content (at% V on metal sublattice) from bottom to top (P0 to P10, respectively). Reference patterns were taken from Ref. [30,31].

smeared diffraction dots (SAED_(b)), or even a ring-like diffraction pattern (SAED_(c)). Together with the respective HR-TEM images (HR-TEM_(b) and HR-TEM_(c)), which indicate narrowing of distinct column boundaries, both HR-TEM and SAED analysis point out that the microstructure transitions into a more nanocrystalline structure with a discontinuous columnar arrangement (highlighted by the x in the

 $HR\text{-}TEM_{(c)}$ image of Fig. 4).

3.2. Structural evolution in relation to V-content

Fig. 5 features X-ray diffractograms and peak-patterns for the as-deposited $Al_{0.7}Cr_{0.3-x}V_xN$ samples P0 to P10. Analogous to Fig. 3, the vanadium contents and chamber locations are listed next to each diffractogram with increasing V-content from bottom to top.

The Al_{0.7}Cr_{0.3}N base system with no vanadium content (P0) features a face-centered-cubic (fcc) crystal structure and exhibits a single-phase Cr(Al)N solid solution with mixed [111]/[200] growth orientations. As chromium is replaced by vanadium in the AlCrN-base-system, the crystal lattice is able to maintain the fcc-Cr(Al,V)N solid solution up to a vanadium content of 6.4 at% on the metal sublattice (P1 = 5.1 at% V and P2 = 6.4 at% V). However, as more vanadium is added (P3 = 8.1 at %), the solubility limit for Al in the fcc-Cr(Al,V)N structure is reached, and the formation of the wurzite-Al(Cr,V)N phase is favored. Consequently, from P4 (10.7 at% V) to P9 (17.4 at% V), a dual-phase, consisting of the fcc-Cr(Al,V)N and w-type Al(Cr,V)N phases make up the coating structures. While we identify the onset for the formation of w-Al (Cr,V) at a V-content of about 8.1 at% (Fig. 5, P3) and the formation of a dual-phase crystal structure thereafter (Fig. 5, P4 to P10), we can relate the competitive growth orientations between the w-Al(Cr,V)N and fcc-Cr(Al,V)N to the gradual grain-refinement first observed at P4 (Fig. 3). Based on this, we propose that the nucleation of the competitive w-Al (Cr,V)N phase with increasing V-content inhibits the growth of the opposing fcc-Cr(Al,V)N crystallites.

Also interesting is the maximum phase-fraction of the w-type Al(Cr, V)N to fcc-Cr(Al,V)N peaking at 15 at% V (P6), after which the fcc-Cr (Al,V)N or rather fcc-V(Cr,Al)N phase is again stabilized and the w-type Al(Cr,V)N phase recedes. This observation is solely made upon the intensity-evolution of the predominant w-AlN 002 reflex.

3.3. Electrochemical corrosion properties

Tafel-plots of the bare 90MnCrV8 alloy (low alloy steel) and as-deposited $Al_{0.7}Cr_{0.3-x}V_xN$ coated samples are shown in Fig. 6a. Tafel-extrapolations were made manually with no additional software package for data analysis. From the intersection of the anodic and cathodic Tafel-branches the corrosion currents (I_{corr}) and corrosion potentials (E_{corr}) have been determined for all samples (listed in Table 1).

3.4. Current density vs. V-content

Firstly, the corrosion currents (i_{corr}) and passivation currents (i_{pass}) that were measured decrease significantly with increasing vanadium-to-chromium-ratio. Whereas quite similar i_{corr} values were obtained for the uncoated alloy and the Al_{0.7}Cr_{0.3}N-coated samples with 0 at% V-content (3.17 $\times 10^{-6}$ and 3.32×10^{-6} A/cm², respectively), a gradual reduction of the corrosion current densities was measured in accordance with the substitution of chromium with vanadium. In more detail, for a V-content of 5.1 at% on the metal sublattice (P1), I_{corr} was determined to be 1.23×10^{-6} A/cm², whereas for V-contents of 11.6 and 22.3 at% (P7 and P10), the measured I_{corr} values decreased to 6.01 \times 10 $^{-7}$ and 9.81×10^{-8} A/cm², respectively.

3.5. Corrosion potential vs. V-content

Secondly, a significant positive shift of the $E_{corr.}$ can be observed from the uncoated alloy (low alloy steel= $-569\,\mathrm{mV_{ssc}}$) to all $Al_{0.7}Cr_{0.3-x}V_xN$ coated samples (P0 = $-354\,\mathrm{mV_{ssc}}$), which indicates a reduced anodic activity of the coated sample over the bare alloy. Further positive shifting of the $E_{corr.}$ is measured as the vanadium-to-chromium-ratio increases for the $Al_{0.7}Cr_{0.3-x}V_xN$ coatings. The most noble $E_{corr.}$ is therefore obtained by the coating with 22.3 at% V on the metal sublattice (P10 = $-148\,\mathrm{mV_{SSC}}$). At this point, we again would like to point

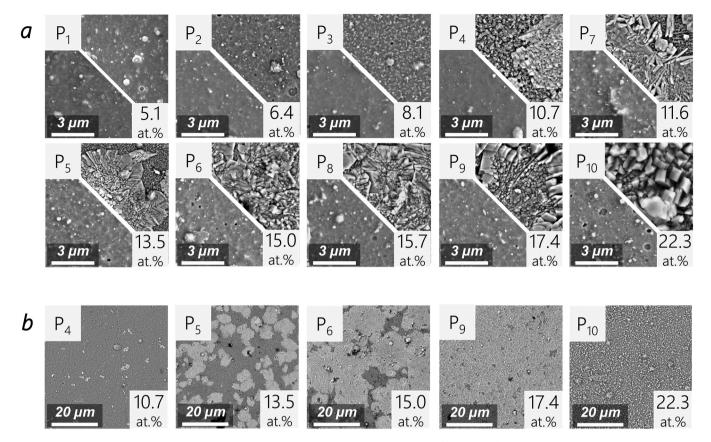


Fig. 8. : SEM top-view images of $Al_{0.7}Cr_{0.3-x}V_xN$ coatings with varying V-contents (at% V on metal sublattice): a) shows combined images consisting of as-deposited (bottom) and annealed states (top, 700 °C for 3 h in air). b) features selected annealed coating surfaces at lower magnification.

out that the measured $E_{\rm corr.}$ for all coated samples are mixed potentials between the coating and substrate material, owed to open porosities and coating defects.

3.6. Open Porosity vs V-content

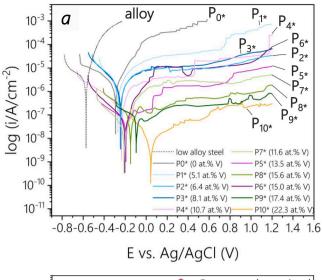
When considering that porosities and fast track diffusion sites along incoherent grain boundaries contribute to a more anodically active galvanic couple (coating/alloy), control over the open porosity of protective coatings is of great importance [1]. Therefore, we would like to put the aforementioned electrochemical data in context with the open porosity values (Eqs.1–2). Fig. 6b shows a bar chart visualizing the correlation between the V-content the open porosity (P_{Rp}) and the polarization resistance (P_{Rp}) of all as-deposited coatings. Standing in good agreement with the SEM and TEM analysis, a gradual decrease in the open porosity rate (P_{Rp}) is observed with increasing V-content. Naturally, with less contact area between the electrolyte and the substrate alloy, the polarization resistance of the coating/substrate couple increases with increasing V-content. All values are also listed in Table 1.

3.7. Isothermal annealing of $Al_{0.7}Cr_{0.3-x}V_xN$ coatings

Now that the microstructure, open porosity, and corrosion behavior have been thoroughly discussed in light of the vanadium content in the $Al_{0.7}Cr_{0.3-x}V_xN$ coatings, we wish to further investigate the corrosion resistance of their respective annealed states. With the goal to develop a vanadium-rich top-oxide scale — intended to function as an additional sealing barrier and to minimize fast-track diffusion junctions to the coating-substrate interface — we first investigated the oxidation behavior of the annealed coatings. Fig. 7 shows the Bragg-Brentano X-ray diffractograms for $Al_{0.7}Cr_{0.3-x}V_xN$ samples P0 to P10, that have been annealed isothermally at 700 °C for 3 h in air. As 700 °C is well below

the phase transition temperature of fcc-Cr(Al)N to w-Al(Cr)N (>900 °C) for the Al_{0.7}Cr_{0.3}N system, we can assume that the overall phase-stability of the Al_{0.7}Cr_{0.3-x}V_xN remains stable throughout the annealing treatment [28]. Moreover, 700 °C also falls well below the oxidation temperature of the fcc-Al_{0.7}Cr_{0.3}N system, where temperatures of > 900 °C have been reported necessary for producing Cr₂O₃ and Al₂O₃ scales [29]. We therefore expect a distinct vanadium threshold content, where predominantly vanadium-oxides form upon annealing at 700 °C. Analogous to the XRD analysis of the as-deposited coatings (Fig. 5), the vanadium contents (at% V on metal sublattice) are listed next to each diffractogram with increasing V-content from bottom to top, together with their respective deposition chamber positions. A reduced corridor of diffraction angles was chosen for the illustration, as i) most of the oxides, $(Cr_2O_3, Al_2O_3, VO, V_nO_{2n+1}, V_nO_{2n-1}, V_nO_{2n})$ feature their prominent Bragg diffractions between 15 and 30 degrees, and ii) any diffraction reflexes larger than 30° would overlap with the fcc-Cr(Al,V)N and w-Al(Cr,V)N peaks [25-27,30-36]. Evident from the diffractograms in Fig. 7, no oxide peak was detected for any of the annealed Al_{0.7}Cr_{0.3-x}V_xN coatings with a V-content up to 8.1 at% (P0 to P3). At a V-content of 10.7 at%, however, first indications of oxidation are noticeable (P4). A similar V-threshold has been reported by Tillmann et. al., observing an oxidation onset at 10.7 at% V, however, with slightly different Al and Cr metal ratios [37]. At V-contents of 11.6 at% and higher, significant oxidation of the coating surfaces is measured with the most prominent Bragg-reflexes identified as a mixed anorthic-AlVO₄ and orthorhombic-V₂O₅ scale.

This sudden onset of the mixed V-oxide evolution is also observed by SEM-analysis. Fig. 8a shows combined top-view images of the asdeposited (bottom half) and its respective annealed coating surfaces (top-half) for all vanadium containing $Al_{0.7}Cr_{0.3-x}V_xN$ coated samples. Standing in good agreement with the XRD measurements, a distinct onset of a developing surface-oxide is seen for the sample P4 (10.7 at% V



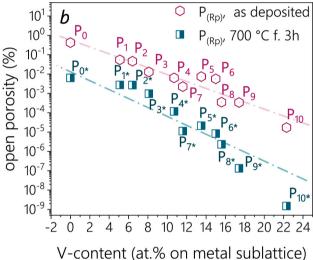


Fig. 9. : Electrochemical data of $Al_{0.7}Cr_{0.3-x}V_xN$ -coated steel samples with varying V-content (at% on metal sublattice) annealed at 700 °C in air: a) Tafel plots and b) calculated open-porosity values for all $Al_{0.7}Cr_{0.3-x}V_xN$ coatings in their as-deposited state, as well as annealed state.

on metal sublattice), where nucleation-islands of vanadium-oxides stud the coating surface. At slightly higher vanadium-concentrations (11.6 at % V on metal sublattice, P7), a converging of the nucleation islands results in a more pronounced oxide scale, which develops thicker and more matured as more vanadium is available within the $Al_{0.7}Cr_{0.3-x}V_xN$ system (P5, P6, P8 and P9). Finally, with a V-content of 22.3 at% on the metal sublattice (P10), distinct vanadium oxide crystals grow, that appear more ordered than the oxide scale at lower V-contents.

Another interesting effect, related to the V-content, is observed at slightly lower magnification, see Fig. 8b. While all samples have been annealed for the same duration of 3 h at 700 °C, a faster growth of the vanadium-oxides-islands is featured for coatings with higher V-contents. While only remote nucleation sites of surface oxides are observed at a V-contents of 10.7 at% on the metal sublattice (P4), considerable spawning of vanadium-oxide patches evolve at a V-content of 13.5 at% (P5). At even higher V-contents (15.0 at% and 17.4 at% V on metal sublattice for P6 and P9, respectively), larger oxide islands develop, which converge to fully cover the coating surface. This is the case for P10 (22.3 at% V on metal sublattice), where a continuous and crystalline vanadium oxide scale has developed on top of the coating.

3.8. Electrochemical investigations of annealed $Al_{0.7}Cr_{0.3-x}V_xN$ -coated samples

LSV measurements of the annealed samples were conducted in an identical manner to the electrochemical investigations of the asdeposited Al_{0.7}Cr_{0.3-x}V_xN coated samples. Fig. 9a shows the Tafelplots of the isothermally annealed Al_{0.7}Cr_{0.3-x}V_xN coated samples, as well as the bare alloy (not annealed). As the V-content of the coatings increases, a shifting of the E_{corr.} into more positive potentials is observed, accompanied by an anew decreasing in the corrosion currents (icorr). Tafel-extrapolations again provide the electrochemical parameters, such as cathodic and anodic Tafel-slopes (β_c and β_a , respectively), corrosion current densities (i_{corr}) and corrosion potentials (E_{corr.}), that were then used for calculating the coatings' porosities (according to Eq. 1 and Eq. 2). The porosity values for all as-deposited and annealed Al_{0.7}Cr_{0.3-x}V_xN samples are plotted in Fig. 9b, with the intention to better illustrate the improved values between the as-deposited and annealed states, as well as to further highlight the beneficial effect of the V-content. A summary of the extrapolated electrochemical values, as well as the calculated values, such as polarization resistance and open porosities are also listed in Table 2.

Lastly, corrosion rates of the as-deposited, as well as annealed coated steel samples were calculated. As there are no indications of dissolution or oxidation processes of the coating material, it is expected that the current densities measured during the electrochemical experiments must come from the low alloy steel substrate (dissolution of iron). In this case, together with Faraday's Law, the mass-loss of the substrate was calculated by correlating the corrosion currents (icorr) with the dissolution of iron (Eq. 3 and Eq. 4). Fig. 10 shows the individual corrosion rates (mg/cm² per year) for each $Al_{0.7}Cr_{0.3-x}V_xN$ -steel couple. Evident is the gradual reduction in mass-loss with increasing V-content within the coatings and an even further reduction in the corrosion rate for the annealed series. With the exception of the as-deposited $Al_{0.7}Cr_{0.3}N$ coating (P0, 0 at% V), all $Al_{0.7}Cr_{0.3-x}V_xN$ coated steel samples exhibit reduced corrosion rates over the uncoated steel substrate.

Reason for this slightly increased corrosion rate of the Al_{0.7}Cr_{0.3}N coated samples, despite the intended protective character of the coating, is the galvanic couple that forms when the electrolyte makes contact with both, the coating matrix and the steel substrate. The more noble coating surface thereby acts as the cathode, whereas the steel-substrate adopts the role of the anode. Due to the vastly larger contact area made between the coating surface (large cathode) compared to the small contact area made between the diffused electrolyte and the steel alloy (small localized anode), accelerated oxidation occurs. As vanadium quite drastically refines the morphology of the Al_{0.7}Cr_{0.3-x}V_xN system, it yields fewer porosities (direct diffusion pathways) for the NaClelectrolyte to reach the coating-substrate interface. Accordingly, with fewer contact area between the electrolyte and the steel substrate, lower corrosion currents (corrosion rates) are generated. We therefore see a strong correlation between the open-porosity values and the calculated corrosion rates of the Al_{0.7}Cr_{0.3-x}V_xN-steel couples.

3.9. Vanadium-oxide scale investigation by TEM

To further answer why the annealed $Al_{0.7}Cr_{0.3-x}V_xN$ sample with the highest V-content (P10 w. 22.3 at% V) performs best in light of its corrosion resistance, additional TEM analysis have been conducted. Here, the aim was to verify the crystal-structures that have been identified by XRD measurements in earlier sections, as well as to take a closer look at the diffusion profiles that evolved during the annealing process. For this, SAEDs together with TEM bright-field images of the coating's surface near region provide localized information about the crystal structure and crystallinity. Shown in Fig. 11a is a bright-field TEM image, which highlights three distinctly different morphologies: a crystalline top-oxide, a nanocrystalline oxygen enriched band underneath, and the pristine coating matrix at the bottom (as found in the as deposited state).

Table 2 Electrochemical properties of annealed $Al_{0.7}Cr_{0.3-x}V_xN$ coated low-alloy steel substrates in 0.1 M NaCl solution. $E_{corr.}$, corrosion potential; I_{pass} , passive current density; i_{corr} , corrosion current density; β_c , cathodic Tafel-slope; β_a , anodic Tafel-slope; R_p , polarization resistance; P_{Rp} , open porosity deduced from R_p .

material	V-content on metal- sublattice (at%)	E _{corr.} (mV)	$I_{pass.}$ (A/cm^2)	I_{corr} (A/cm^2)	βc (mV/dec)	βα (mV/dec)	R_p $(k\Omega \times cm^2)$	porosity (%)
$Al_{0.7}Cr_{0.3-x}V_xN$ annealed at 700 °C f. 3 h in	0 (P0*)	-291	$\begin{array}{c} 2.61{\times}10^{-4} \\ \pm 1.81{\times}10^{-5} \end{array}$	4.39×10^{-6}	127.6	67.2	43.1	6.34×10^{-3}
	5.1 _(P1*)	-269	$\begin{array}{l} 2.23 \times 10^{-5} \\ \pm 2.03 \times 10^{-6} \end{array}$	3.60×10^{-7}	86.1	86.5	51.1	2.75×10^{-3}
	6.4 _(P2*)	-248	8.80×10^{-6} $\pm 8.12 \times 10^{-7}$	8.99×10^{-7}	108.0	127.8	27.9	2.70×10^{-3}
	8.1 _(P3*)	-242	$5.96 \times 10^{-6} $ $\pm 7.54 \times 10^{-7}$	2.45×10^{-7}	93.4	61.8	65.2	9.66×10^{-4}
	10.7 _(P4*)	-233	$1.72 \times 10^{-6} \\ \pm 1.79 \times 10^{-7}$	3.31×10^{-8}	117.4	43.1	408.9	1.18×10^{-4}
	11.6 _(P7*)	-210	$6.79 \times 10^{-7} \\ \pm 1.13 \times 10^{-7}$	2.30×10^{-8}	128.4	102.1	1132.0	2.13×10^{-5}
	13.5 _(P5*)	-194	$1.72 \times 10^{-6} \ \pm 6.38 \times 10^{-7}$	9.15×10^{-9}	92.9	65.1	1794.4	8.34×10^{-5}
	15.0 (P6*)	-203	$4.90 \times 10^{-6} \pm 1.08 \times 10^{-6}$	8.58×10^{-9}	74.2	66.3	1751.5	1.12×10^{-5}
	15.6 _(P8*)	-147	$1.40 \times 10^{-7} $ $\pm 3.60 \times 10^{-8}$	1.60×10^{-8}	111.5	124.8	1580.9	2.32×10^{-6}
	17.4 _(P9*)	-95	$5.26 \times 10^{-8} \ \pm 2.64 \times 10^{-8}$	8.18×10^{-9}	181.8	283.3	5813.9	1.33×10^{-7}
	22.3 (P10*)	-47	$1.61 \times 10^{-8} \\ \pm 1.58 \times 10^{-9}$	1.59×10^{-9}	129.2	206.6	21,511.0	1.50×10^{-9}

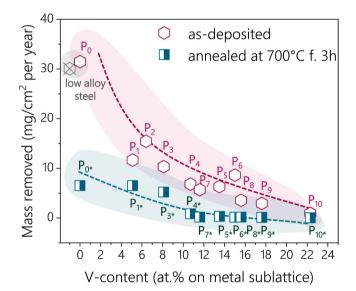


Fig. 10.: Comparison of the corrosion rates of as-deposited $Al_{0.7}Cr_{0.3-x}V_xN$ coated and annealed $Al_{0.7}Cr_{0.3-x}V_xN$ coated low-alloy steel substrates with varying V-contents (at% V on metal sublattice).

Starting with the top-oxide, single-crystalline domains are detected, as is evident from the spot-pattern of the SAED_a in Fig. 11b. Indexing of the pattern renders a triclinic (anorthic) crystal structure of the AlVO₄-oxide with the space group $P\overline{1}$, which stands in excellent agreement with the findings from the XRD measurements and results from Franz et. al. [38,39].

Moving below the granular top-oxide, the $SAED_b$ in Fig. 11c features a combination of an amorphous material with a characteristic halo-ring pattern, as well as a nanostructured polycrystalline matrix, with typical smeared diffraction rings that appear further away from the primary beam. The decomposition of the original polycrystalline matrix to a semi-amorphous morphology can be attributed to the oxidation process during annealing, where oxygen inward diffusion is accompanied by

simultaneous dissipation of nitrogen. By integrating the SAEDb ringpattern and plotting it over the reciprocal of the lattice-spacing, an intensity plot with broadened but still defined peaks is generated, which is shown in Fig. 11f. Again, we can deduce that the broadened peaks convey an amorphous character of the coating matrix, whereas more defined [200] and [220] reflexes of the fcc-CrN crystal structure suggest residue fragments of the original coating structure. The fact that only fcc-CrN residues appear in the intensity plot suggests a faster degradation mechanism of the hexagonal phase fraction, which greatly affects the diffusion of oxygen and other alloyed elements, such as vanadium. Lastly, SAED_c and SAED_d are intended to show the pristine dual fcc-Cr (Al,V)N and w-type Al(Cr,V)N phases. Furthermore, they reveal significant differences in the crystallinity of the coating morphology that is in close proximity of the oxygen-diffusion front (SAED_c) and the morphology that is further away (SAED_d). Evident from SAEDs in Fig. 11d and Fig. 11e, similar diffraction rings are obtained, whose integration in Fig. 11f also show close to identical intensity plots and, as expected, render the correct D-spacings for the fcc-Cr(Al,V)N and w-Al (Cr,V)N crystal structures. We therefore conclude that there is a sharp oxygen diffusion front, with little to no lattice distortion after.

3.10. Description of diffusion mechanisms

Next, the diffusion mechanisms are investigated in more detail. In accordance with the TEM analysis in Fig. 11, the same region of the annealed sample is chosen. First, we would like to direct the reader's attention to a top view SEM image in Fig. 12a and emphasize that the entire coating surface is homogeneously studded with a highly crystalline AlVO₄ top-oxide, which is otherwise not apparent from other cross-section images. Fig. 12b then shows a scanning TEM (STEM) image of the cross-section, which was chosen for subsequent EDX analysis. Several defined layers are visible through the generated mass contrast of the different coating domains. While areas with heavier elements appear brighter, regions with lighter elements produce a darker contrast in the image. First, an EDX line-scan was conducted across the entire field of view in order to take a closer look on the oxygen diffusion profile (Fig. 12c). Clearly evident is the sudden drop at the oxygen diffusion front (as labeled in Fig. 12b), where a simultaneous surge of nitrogen is

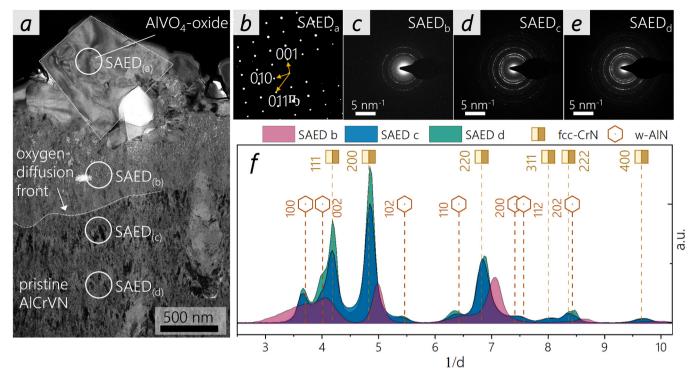


Fig. 11. : TEM investigations highlighting the oxidation behavior of $Al_{0.7}Cr_{0.08}V_{0.22}N$ coating isothermally annealed at 700 °C in air for 3 h. a) shows a bright-field image, highlighting the most prominent structural features, as well as the positions of $SAED_{(a-d)}$ measurements. (b-e) show the SAED-patterns that originate from the positions labeled in sub-figure (a). f) features the integrated ring-patterns from $SAED_{(b-d)}$.

recorded. This coincides with the understanding that there is a sharp interface between the oxidized coating and the remaining pristine coating matrix underneath. Also evident is a vanadium depletion layer, which results from an outward diffusion of vanadium in order to form a crystalline AlVO₄-top oxide. These migration dynamics become clearer when looking at the individual EDX maps in Fig. 12d. The respective nitrogen and oxygen maps substantiate the sharp interface between the oxidized coating and the remaining pristine coating morphology. Moreover, a distinct vanadium depletion layer is shown. Standing in good agreement with the findings from the line-scan, the presence of the depletion layer suggests an outward directed diffusion of vanadium for the formation of the AlVO₄-oxide. Chromium also indicates outward directed diffusion, however only to a marginal degree. As Cr does not participate in the formation of a top oxide, it instead concentrates at the grain-boundaries of the AlVO₄-crystals as shown in Fig. 12c, as well as EDX map of 12d. Lastly, aluminum shows little migration across the oxygen/nitrogen diffusion-front. This observation suggests that sufficient aluminum is originally present for the formation of the AlVO₄-top oxide, with no chemical gradient that will instigate further Al diffusion to the surface.

3.11. Overview of electrochemical parameters of various coating systems

Lastly, we wish to place the corrosion resistance of the presented $Al_{0.7}Cr_{0.3-x}V_xN$ coatings into context with other material-systems deposited by this research group. Fig. 13 shows an overview of I_{corr} vs. E_{corr} values of various coating materials deposited on low alloy steel (90MnCrV8) that have been electrochemically tested in an identical manner, as described in the previous experimental section (deposition parameters and electrochemical data can be found in Appendix B). Quite evident is the significant spread of i_{corr} and E_{corr} values across the presented material classes. However, also within a family, such as the nitrides, significant variance in the electrochemical behavior is present, proving just how sensitive corrosion resistance of PVD coatings is to slight changes chemical composition and/or coating morphology. With

this overview, we would like to emphasize the need for more detailed investigations devoted to specific material families, in order to systematically improve the corrosion resistance of PVD coatings in NaCl-rich media. Moreover, we would like to stress that both, alloying strategies and post deposition treatments such as annealing in air, pose viable approaches in significantly improving the corrosion resistance of cathodic arc evaporated $Al_{0.7}Cr_{0.3-x}V_xN$ coatings.

4. Conclusion

To improve the corrosion resistance of cathodic arc evaporated AlCrN-based coatings in NaCl-rich media, this study has provided two effective approaches: i) a doping-strategy with vanadium, and ii) an annealing strategy at 700 $^{\circ}\text{C}$ in air for 3 h.

In a deposition series of Al_{0.7}Cr_{0.3-x}V_xN coatings, a direct correlation was found between the V-content, the coatings' crystallinity, and their corrosion current densities during electrochemical investigation. With increasing vanadium fractions, more refined coating morphologies were obtained, as well as lower current densities during the corrosion experiments. We propose that the reason for the progressive grain refinement is attributed to the nucleation of the favorable w-Al(Cr,V)N phase at higher vanadium contents, which inhibits the growth of the opposing fcc-Cr(Al,V)N crystallites. As a result, diffusion paths from the coating surface to the coating-substrate interface become increasingly branched, as more grain boundaries impede the migration of the electrolyte through the coating. In a series of 10 Al_{0.7}Cr_{0.3-x}V_xN coatings with varying V-contents, ranging from 5.1 to 22.3 at% on the metal sublattice, each raise in the V-fraction lowered the corrosion currents noticeably, and resulted in a positive shift of the respective corrosion potential. Using the Stern-Geary equation together with the assumption that the coating material remains inert throughout the electrochemical experiment (only the steel substrate accounts for the anodic current), an approximation of the coatings' open porosity was made [3]. Appropriately, the approximation revealed a significant decline in the coatings' porosity values, which is a result of the observed grain-refinement due to

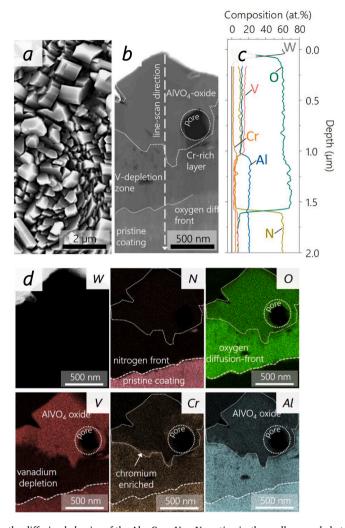


Fig. 12. : EDX investigations highlighting the diffusion behavior of the $Al_{0.7}Cr_{0.08}V_{0.22}N$ coating isothermally annealed at 700 °C in air for 3 h. a) shows a top-view SEM image of the crystalline top-oxide. b) features a STEM cross-section image of the top-most section of the annealed coating with the most prominent features labeled. c) displays an EDX-line scan that belongs to the segment shown sub-figure (b). d) displays EDX-maps, originating from the same segment as shown in sub-figures (b and c).

increasing V-fractions.

Moreover, a second series of $Al_{0.7}Cr_{0.3-x}V_xN$ coatings with V-contents ranging from 5.1 to 22.3 at% on the metal sublattice was annealed at 700 °C for 3 h in air and electrochemically tested in a 0.1 M NaCl-solution. For all annealed samples, significant shifting of the $E_{corr.}$ into more positive potentials was measured, accompanied by an anew decreasing in the corrosion currents (i_{corr}). Compared with the electrochemical values from the doping strategy, further improvement was obtained through the additional annealing step at 700 °C. We attribute this enhanced corrosion resistance to the formation of a \sim 1 µm thick AlVO₄-top oxide, followed by a \sim 0.5 µm thick oxygen-enriched (vanadium depleted) nanocrystalline layer underneath. We propose that this combination of top-oxide formation and formation of a near amorphous oxygen enriched layer below, drastically reduces the open-porosity rates of the coating structure as a whole and renders improved corrosion protection.

CRediT authorship contribution statement

O. E. H. and H. R. conceived the research. O. E. H. conducted the coating depositions, as well as the electrochemical corrosion tests. P. K.

prepared the TEM lamellas, whereas T. W. conducted the TEM measurements. E. N. and D. P. conducted the ToF-HIERDA measurements. O. H. and P. P. supported the research by providing indispensable funding, while L. S., J. R., and S. K. assisted the research with their thematic expertise. H. R. also provided funding acquisition and oversaw the research as supervisor. Finally, all authors have contributed in revising and approving the final version of the manuscript.

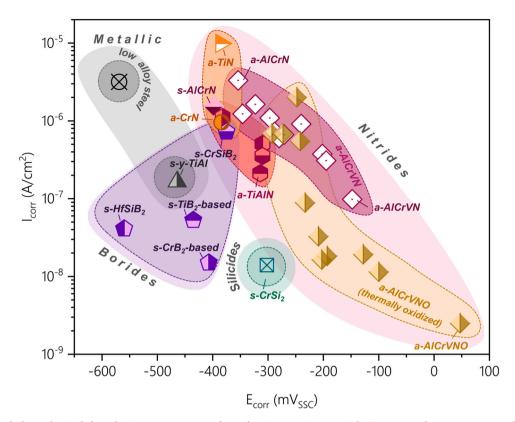
Declaration of Competing Interest

The authors declare the following financial interests/personal relationships which may be considered as potential competing interests: Oliver E. Hudak reports financial support was provided by Christian Doppler Research Association.

Data Availability

Data will be made available on request.

2



 $\textbf{Fig. 13.:} \ \text{Summarized electrochemical data showing } I_{corr} \ vs. \ E_{corr} \ values \ of \ various \ coating \ materials \ (s = sputtered, \ a = \ arc \ evaporated) \ measured \ in \ 0.1 \ M$ NaCl solution.

Table A1 Overview showing the chemical compositions of the as-deposited Al_{0.7}Cr_{0.3-x}V_xN coatings. All listed values reflect EDX measurements that have been corrected according to ERDA measurements. Accordingly, ERDA values from samples P4 and P10, with compositions equivalent to $Al_{0.32}(Cr, V)_{0.19}N_{0.49}$, provided the correction standard.

sample	V- content (at%)	Al- content (at%)	Cr- content (at%)	N- content (at%)	impurities (Oxygen) (at%)	Al- content on metal sublattice (at%)	Cr-content on metal sublattice (at%)	V- content on metal sublattice (at%)
PO	0.0	32.8	14.9	48.9	3.5	68.8	31.2	0.0
P1	2.7	34.7	15.9	45.5	1.2	65.1	29.8	5.1
P2	3.2	32.5	14.5	47.2	2.5	64.7	28.9	6.4
P3	4.0	32.7	13.2	47.4	2.6	65.5	26.4	8.1
P4	5.2	32.4	10.9	48.2	3.2	66.8	22.5	10.7
P5	7.2	31.9	9.1	48.4	3.3	66.1	18.9	15.0
P6	6.6	31.4	10.6	48.2	3.2	64.7	21.8	13.5
P7	5.6	31.4	11.2	48.4	3.3	65.1	23.3	11.6
P8	7.6	30.5	10.4	48.3	3.3	63.3	21.4	15.6
P9	8.4	30.7	9.4	48.2	3.2	63.3	19.4	17.4
P10	10.6	30.3	6.5	48.9	3.7	63.9	13.8	22.3

Table A2 Overview of deposition parameters, as well as electrochemical parameters ($I_{corr.}$ and $E_{corr.}$) measured in 0.1 M NaCl solution, pertaining to Fig. 13.

sample	deposition technique	T_{dep} (C°)	P _{dep.} (Pa)	atmosphere	bias (V)	$I_{dep.}$ (A)	ref.	$E_{corr.}$ (mV)	I_{corr} (A/cm^2)
AlCrN	cae	480	3.5	N_2	≥ −100		[1]	-375	2.57×10^{-6}
AlCrVN	cae	480	3.5	N_2	≥ -100		-	-148	$1.03 imes 10^{-7}$
AlCrVNO	cae	480	3.5	N_2	≥ -100		-	-47	1.59×10^{-9}
CrN	cae	500	3.5	N_2	-80	150	[40]	-384	9.57×10^{-7}
TiN	cae	500	0.8	N_2	-80	160	[40]	-385	9.89×10^{-6}
TiAlN	cae	500	3.0-3.2	N_2	-40 to − 80	200	[40,41]	-314	2.12×10^{-7}
AlCrN	sputtering	500	1.3	Ar/N_2	-160		[1]	-398	$1.54 imes 10^{-6}$
y-TiAl	sputtering	<i>≤ 300</i>	0.4	Ar	-50	-	[42]	-464	1.65×10^{-7}
$HfSiB_2$	sputtering	550	0.56	Ar	-40	0.4	[43]	-560	4.11×10^{-8}
TiB_2 -based	sputtering	500	0.4	Ar	-50	0.4	[44]	-435	5.29×10^{-8}
CrB_2 -based	sputtering	550	0.7	Ar	-40	0.4	[45]	-407	1.50×10^{-8}
$CrSiB_2$	sputtering	550	0.56	Ar	-40	0.5	[43]	-375	7.24×10^{-7}
CrSi ₂	sputtering	400	0.4	Ar	-50	0.4		-302	1.40×10^{-8}

Acknowledgments

The financial support by the Austrian Federal Ministry for Digital and Economic Affairs, the National Foundation for Research, Technology and Development and the Christian Doppler Research Association is gratefully acknowledged (Christian Doppler Laboratory "Surface Engineering of high-performance Components"). We also thank for the financial support of Plansee SE, Plansee Composite Materials GmbH, and Oerlikon Balzers, Oerlikon Surface Solutions AG. In addition, we want to thank the X-ray center (XRC) of TU Wien for beam time as well as the electron microscopy center - USTEM TU Wien - for providing the SEM and TEM facilities. The authors acknowledge TU Wien library for financial support through its Open Access Funding Program.

Appendix

See Table A1 and A2.

References

- [1] O.E. Hudak, A. Bahr, P. Kutrowatz, T. Wojcik, F. Bohrn, L. Solyom, R. Schuster, L. Shang, O. Hunold, P. Polcik, M. Heller, P. Felfer, G. Ball, H. Riedl, Pitting corrosion – Preferred chloride diffusion pathways in physical vapor deposited AlCrN coatings, Corros. Sci. 211 (2023), 110901, https://doi.org/10.1016/j. corsci.2022.110901.
- [2] A.Y. Adesina, Z.M. Gasem, A. Madhan Kumar, Corrosion resistance behavior of single-layer cathodic Arc PVD nitride-base coatings in 1M HCl and 3.5 pct NaCl solutions, Metall. Mater. Trans. B Process Metall. Mater. ProcessSci 48 (2017) 1321–1332, https://doi.org/10.1007/s11663-016-0891-7.
- [3] B. Avci, K. Kazmanli, B. Evren, M. Urgen, Contribution of galvanic coupling with TiN, TiAlN, and CrN to the corrosion of steel in neutral and acidic chloride solutions, Mater. Corros. (2023) 1–10. https://doi.org/10.1002/maco.202313848.
- [4] C. Charrier, P. Jacquot, E. Denisse, J.P. Millet, H. Mazille, Aluminium and Ti/Al multilayer PVD coatings for enhanced corrosion resistance, Surf. Coat. Technol. 90 (1997) 29–34, https://doi.org/10.1016/S0257-8972(96)03080-0.
- [5] J. Creus, H. Mazille, H. Idrissi, Porosity evaluation of protective coatings onto steel, through electrochemical techniques, Surf. Coat. Technol. 130 (2000) 224–232, https://doi.org/10.1016/S0257-8972(99)00659-3.
- [6] J. Creus, H. Idrissi, H. Mazille, F. Sanchette, P. Jacquot, Improvement of the corrosion resistance of CrN coated steel by an interlayer, Surf. Coat. Technol. 107 (1998) 183–190, https://doi.org/10.1016/S0257-8972(98)00646-X.
- [7] J. Vega, H. Scheerer, G. Andersohn, M. Oechsner, Experimental studies of the effect of Ti interlayers on the corrosion resistance of TiN PVD coatings by using electrochemical methods, Corros. Sci. 133 (2018) 240–250, https://doi.org/ 10.1016/j.corsci.2018.01.010.
- [8] W. Brandl, C. Gendig, K. Reichel, Corrosion behaviour of hybrid coating systems, Mater. Corros. Werkst. Und Korros. 47 (1996) 208–214, https://doi.org/10.1002/ maco.19960470405
- [9] M. Flores, L. Huerta, R. Escamilla, E. Andrade, S. Muhl, Effect of substrate bias voltage on corrosion of TiN/Ti multilayers deposited by magnetron sputtering, Appl. Surf. Sci. 253 (2007) 7192–7196, https://doi.org/10.1016/j. aps/scc. 2007.02.203
- [10] C. Liu, A. Leyland, Q. Bi, A. Matthews, Corrosion resistance of multi-layered plasma-assisted physical vapour deposition TiN and CrN coatings, Surf. Coat. Technol. 141 (2001) 164–173, https://doi.org/10.1016/S0257-8972(01)01267-1.
- [11] S.H. Ahn, J.H. Lee, H.G. Kim, J.G. Kim, A study on the quantitative determination of through-coating porosity in PVD-grown coatings, Appl. Surf. Sci. 233 (2004) 105–114, https://doi.org/10.1016/j.apsusc.2004.03.213.
- [12] F. Lang, Z. Yu, The corrosion resistance and wear resistance of thick TiN coatings deposited by arc ion plating, Surf. Coat. Technol. 145 (2001) 80–87, https://doi. org/10.1016/S0257-8972(01)01284-1.
- [13] J. Barranco, F. Barreras, A. Lozano, M. Maza, Influence of CrN-coating thickness on the corrosion resistance behaviour of aluminium-based bipolar plates, J. Power Sources 196 (2011) 4283–4289, https://doi.org/10.1016/j.jpowsour.2010.11.069.
- [14] H.A. Jehn, Improvement of the corrosion resistance of PVD hard coating-substrate systems, Surf. Coat. Technol. 125 (2000) 212–217, https://doi.org/10.1016/ S0257-8972(99)00551-4.
- [15] Y. Massiani, A. Medjahed, J.P. Crousier, P. Gravier, I. Rebatel, Corrosion of sputtered titanium nitride films deposited on iron and stainless steel, Surf. Coat. Technol. 45 (1991) 115–120, https://doi.org/10.1016/0257-8972(91)90213-G.
- [16] F. Vacandio, Y. Massiani, M. Eyraud, S. Rossi, L. Fedrizzi, Influence of various nickel under-layers on the corrosion behaviour of AIN films deposited by reactive sputtering, Surf. Coat. Technol. 137 (2001) 284–292, https://doi.org/10.1016/ S0257-8972(00)01110-5.
- [17] M. Nordin, M. Herranen, S. Hogmark, Influence of lamellae thickness on the corrosion behaviour of multilayered PVD TiN/CrN coatings, Thin Solid Films 348 (1999) 202–209, https://doi.org/10.1016/S0040-6090(99)00192-3.

- [18] C.S. Lin, C.S. Ke, H. Peng, Corrosion of CrN and CrN/TiN coated heat-resistant steels in molten A356 aluminum alloy, Surf. Coat. Technol. 146–147 (2001) 168–174, https://doi.org/10.1016/S0257-8972(01)01484-0.
- [19] M. Herranen, U. Wiklund, J.O. Carlsson, S. Hogmark, Corrosion behaviour of Ti/ TiN multilayer coated tool steel, Surf. Coat. Technol. 99 (1998) 191–196, https://doi.org/10.1016/S0257-8972(97)00525-2.
- [20] P.E. Hovsepian, D.B. Lewis, W.D. Münz, S.B. Lyon, M. Tomlinson, Combined cathodic arc/unbalanced magnetron grown CrN/NbN superlattice coatings for corrosion resistant applications, Surf. Coat. Technol. 120–121 (1999) 535–541, https://doi.org/10.1016/S0257-8972(99)00439-9.
- [21] L. Shan, Y.R. Zhang, Y.X. Wang, J.L. Li, X. Jiang, J.M. Chen, Corrosion and wear behaviors of PVD CrN and CrSiN coatings in seawater, Trans. Nonferrous Met. Soc. China (Engl. Ed. 26 (2016) 175–184, https://doi.org/10.1016/S1003-6326(16) 64104-3.
- [22] P. Ström, D. Primetzhofer, Ion beam tools for nondestructive in-situ and inoperando composition analysis and modification of materials at the Tandem Laboratory in Uppsala, J. Instrum. 17 (2022), https://doi.org/10.1088/1748-0221/17/04/P04011.
- [23] M. Janson, CONTES Conversion of Time-Energy-Spectra-A Program for ERDA Data Analysis Users Manual, 2004.
- [24] P. Ström, P. Petersson, M. Rubel, G. Possnert, A combined segmented anode gas ionization chamber and time-of-flight detector for heavy ion elastic recoil detection analysis, Rev. Sci. Instrum. 87 (2016), https://doi.org/10.1063/1.4963709.
- [25] International Center of Diffraction Data, Powder diffraction file 00–046-1200, 1996
- [26] International Center of Diffraction Data, Powder diffraction file 04–014-0360, 2010.
- [27] International Center of Diffraction Data, Powder diffraction file 01–083-5613, 2016
- [28] Y.P. Feng, L. Zhang, R.X. Ke, Q.L. Wan, Z. Wang, Z.H. Lu, Thermal stability and oxidation behavior of AlTiN, AlCrN and AlCrSiWN coatings, Int. J. Refract. Met. Hard Mater. 43 (2014) 241–249, https://doi.org/10.1016/j.ijrmhm.2013.11.018.
- [29] C. Tritremmel, R. Daniel, C. Mitterer, P.H. Mayrhofer, M. Lechthaler, C. Tritremmel, R. Daniel, C. Mitterer, Oxidation behavior of arc evaporated Al-Cr-Si-N thin films, Oxid. Behav. arc evaporated Al-Cr-Si-N. Thin films 061501 (2015), https://doi.org/10.1116/1.4748802.
- [30] International Center of Diffraction Data, Powder diffraction file 00–039-0276,
- [31] International Center of Diffraction Data, Powder diffraction file 01–072-0433, 2020.
- [32] International Center of Diffraction Data, Powder Diffraction file 00–015-0629, 1965.
- [33] International Center of Diffraction Data, Powder Diffraction file 04–001-9278, 2011.
- [34] International Center of Diffraction Data, Powder Diffraction file 04–015-8610, 2012.
- [35] International Center of Diffraction Data, Powder Diffraction File 04–025-1918, 2021
- [36] International Center of Diffraction Data, Powder Diffraction File 01–076-0146, 2020.
- [37] W. Tillmann, D. Kokalj, D. Stangier, M. Paulus, C. Sternemann, M. Tolan, Investigation on the oxidation behavior of AlCrVxN thin films by means of synchrotron radiation and influence on the high temperature friction, Appl. Surf. Sci. 427 (2018) 511–521, https://doi.org/10.1016/j.apsusc.2017.09.029.
- [38] R. Franz, J. Neidhardt, C. Mitterer, B. Schaffer, H. Hutter, R. Kaindl, B. Sartory, R. Tessadri, M. Lechthaler, P. Polcik, Oxidation and diffusion processes during annealing of AlCrVN hard coatings, J. Vac. Sci. Technol. A Vac. Surf. Film. 26 (2008) 302–308, https://doi.org/10.1116/1.2841508.
- [39] R. Franz, J. Schnöller, H. Hutter, C. Mitterer, Oxidation and diffusion study on AlCrVN hard coatings using oxygen isotopes 160 and 180, Thin Solid Films 519 (2011) 3974–3981, https://doi.org/10.1016/j.tsf.2011.01.100.
- [40] C. Sabitzer, C. Steinkellner, C.M. Koller, P. Polcik, R. Rachbauer, P.H. Mayrhofer, Diffusion behavior of C, Cr, and Fe in arc evaporated TiN- and CrN-based coatings and their influence on thermal stability and hardness, Surf. Coat. Technol. 275 (2015) 185–192, https://doi.org/10.1016/j.surfcoat.2015.05.020.
- [41] S.A. Glatz, C.M. Koller, H. Bolvardi, S. Kolozsvári, H. Riedl, P.H. Mayrhofer, Influence of Mo on the structure and the tribomechanical properties of arc evaporated Ti-Al-N, Surf. Coat. Technol. 311 (2017) 330–336, https://doi.org/ 10.1016/j.surfcoat.2017.01.001.
- [42] S. Kagerer, O.E. Hudak, M. Schloffer, H. Riedl, P.H. Mayrhofer, TGO formation and oxygen diffusion in Al-rich gamma-TiAl PVD-coatings on TNM alloys, Scr. Mater. 210 (2022), 114455, https://doi.org/10.1016/j.scriptamat.2021.114455.
- [43] T. Glechner, H.G. Oemer, T. Wojcik, M. Weiss, A. Limbeck, J. Ramm, P. Polcik, H. Riedl, Influence of Si on the oxidation behavior of TM-Si-B2±z coatings (TM = Ti, Cr, Hf, Ta, W), Surf. Coat. Technol. 434 (2022), 128178, https://doi.org/10.1016/j.surfcoat.2022.128178
- [44] C. Fuger, R. Hahn, A. Hirle, P. Kutrowatz, M. Weiss, A. Limbeck, O. Hunold, P. Polcik, H. Riedl, Revisiting the origins of super-hardness in TiB2+z thin films – Impact of growth conditions and anisotropy, Surf. Coat. Technol. 446 (2022), https://doi.org/10.1016/j.surfcoat.2022.128806.
- [45] L. Zauner, A. Steiner, T. Glechner, A. Bahr, B. Ott, R. Hahn, T. Wojcik, O. Hunold, J. Ramm, S. Kolozsvári, P. Polcik, P. Felfer, H. Riedl, Role of Si segregation in the structural, mechanical, and compositional evolution of high-temperature oxidation resistant Cr-Si-B2±z thin films, J. Alloy. Compd. 944 (2023), 169203, https://doi.org/10.1016/j.jallcom.2023.169203.